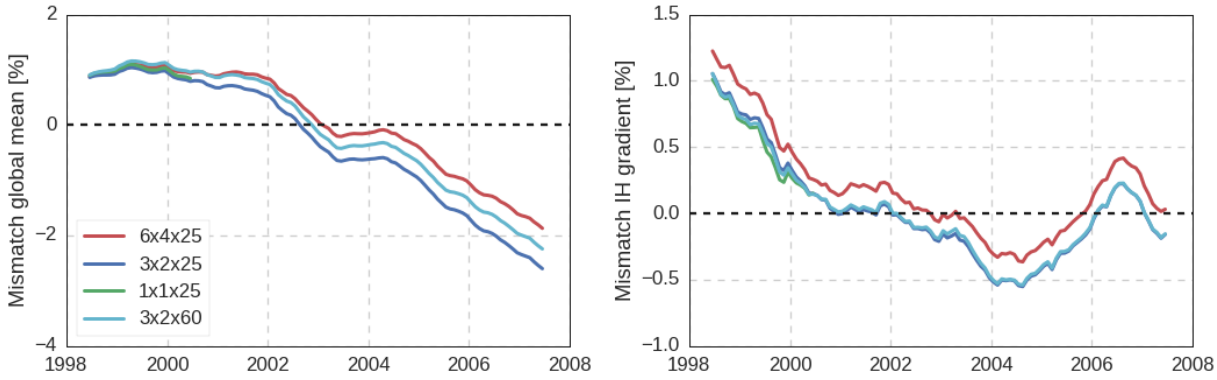

Figure S1: Mismatch between simulated and observed MCF mole fractions in the global mean (left) and the interhemispheric gradient(right), when TM5 is operated at different vertical and horizontal resolutions. The mismatches are given relative to global mean observed MCF and averaged using a twelve-month running mean. Monthly mean hemispheric and global averages were calculated from individual observations of the NOAA surface network, following the procedure described in [1].

Supporting Information to Naus et al. (2020)

S1 High-resolution simulations

We performed the inversions of MCF at the coarsest resolution supported in TM5: 6° longitude by 4° latitude, with 25 vertical levels. TM5 can also be operated at 3° by 2° and at 1° by 1°, with up to 60 vertical levels. The resolution at which a model is operated affects the simulated transport, with a higher resolution generally being associated with more accurate transport. Therefore, we performed forward simulations of MCF at different resolutions to determine the impact of resolution on our inversion results. We performed simulations at 1° by 1° with 25 vertical layers for the 1998-2001 period, and at 3° by 2° with 25 and with 60 vertical layers for the 1998-2008 period. Since the amplitude of the effect was apparent from the first few years of the simulations, we did not simulate the whole period. In these forward simulations, we used the prior settings of the standard inversion set-up.

Figure S1 shows the effect of model resolution on the global mean mixing ratio and the interhemispheric gradient of MCF, as determined from surface sites. We find that with a higher horizontal resolution the global lifetime and the interhemispheric gradient of MCF are slightly reduced. The reduced lifetime is driven by an increase in the secondary sinks, both oceanic loss and stratospheric photolysis. However, the increase in the secondary sinks corresponds to only 0.1% to 0.5% of the total OH sink and is largely time-invariant. Therefore, we deem these effects not important for our derivation of OH variations. Not shown here are the site-to-site gradients, because these were only marginally affected by model resolution.

In conclusion, we find the impact of increased resolution to be small, so that the conclusions derived from the coarse-resolution inversions remain unaffected.

S2 Simulations of SF_6 and HFC-152a

We used the TM5 set-up described in Section to also simulate SF_6 and HFC-152a mole fractions, in a forward simulation from 1998 to 2018. The objective of simulating additional tracers was to diagnose whether the intrahemispheric biases that are apparent for MCF (as discussed in Section 3.4) are specific to MCF, or can also be seen for other tracers. To do this, we sampled a simulation with HFC-152a and SF_6 at the same

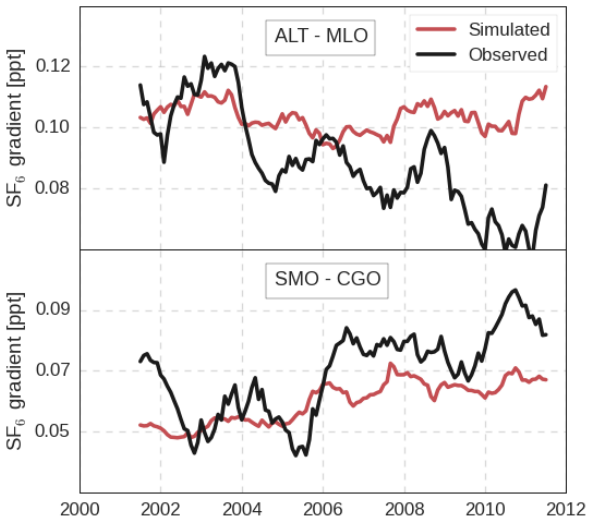

Figure S2: Simulated and observed SF_6 mole fraction gradients between two site pairs. We applied a twelve-month moving average to the monthly mean mole fractions per site.

NOAA surface sites as the MCF simulations. Both HFC-152a and SF_6 are measured in the NOAA HATS network, following the procedures similar to those for MCF, which are described in Section 2.2.1.

S2.1 SF_6

Similar to MCF, SF_6 is emitted only anthropogenically, and its emissions are therefore predominantly located in the Northern mid-latitudes. Atmospheric loss of SF_6 occurs in the upper stratosphere, slowly, resulting in a global lifetime of >1000 years [2]. Atmospheric gradients of SF_6 are therefore solely determined by emissions and transport. Given reasonable constraints on SF_6 emissions, the atmospheric distribution of SF_6 is a good proxy for large-scale atmospheric transport [3] [4]. In our simulations, we used emission fields described in the TransCom Age of Air project [5], with no loss process implemented. In [5] it was shown that these emissions, when implemented in TM5, realistically reproduce the global evolution of SF_6, as well as its interhemispheric gradient.

Figure S2 shows the simulated and observed intrahemispheric SF_6 gradients between ALT and MLO in the Northern Hemisphere, and between SMO and SPO in the Southern Hemisphere. These gradients can be compared to Figure 5 for MCF. We are able to reproduce the intrahemispheric gradients of SF_6. For MCF, we found intrahemispheric gradients to be underestimated by 20-30%. If this were related to a transport bias in TM5, then mixing within the hemispheres would be too fast, and intrahemispheric gradients of SF_6 should also be systematically underestimated. We do find some multi-annual differences between observed and simulated SF_6 mole fraction gradients, but these differences are of opposite sign in both hemispheres and do not persist over the whole twenty-year period, which points to other error sources (e.g. the emission distribution). Therefore, we deem it unlikely that a transport bias is the dominant driver of the underestimate of MCF intrahemispheric gradients.

S2.2 HFC-152a

HFC-152a is an anthropogenically emitted gas, used mainly as an aerosol and foam-blowing agent. The dominant atmospheric loss process of HFC-152a is its reaction with OH, resulting in a global lifetime of

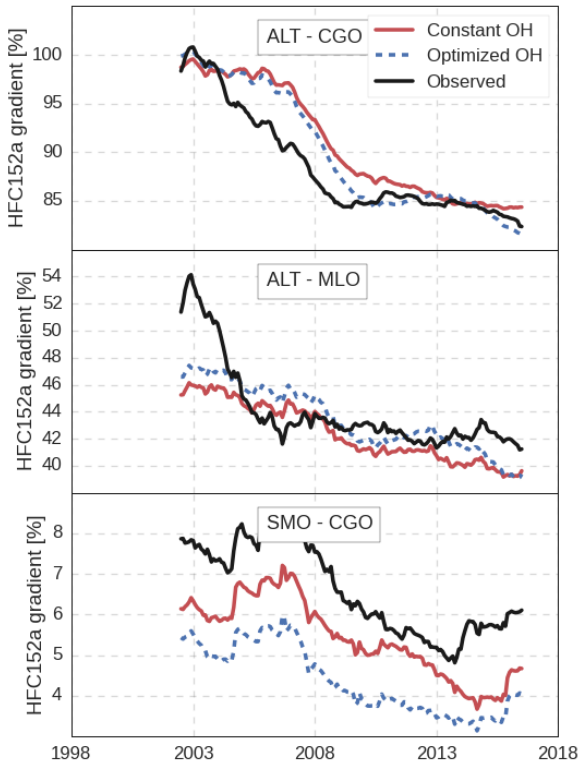

Figure S3: Simulated and observed HFC-152a mole fraction gradients between three site pairs. We applied a twelve-month moving average to the monthly mean mole fractions per site and we calculated the fractional gradients relative to the global mean mole fraction of HFC-152a.

1.6 years [6]. In [7], HFC-152a was proposed as a tracer for OH, alternative (or complimentary) to MCF. HFC-152a was shown to be especially sensitive to the seasonality and to the interhemispheric ratio of OH, partly due to its shorter lifetime compared to MCF. Most countries report HFC-152a emissions, but often aggregated with emissions of other HFC's. Additionally, atmospheric observations indicate that HFC-152a emissions, as reported in these bottom-up inventories, are significantly too low [8]. We used emission maps provided in the EDGAR v4.2 inventory, which are available up to 2008. For later years, we repeated the 2008 distribution. We adopted annual emission totals from [8], which approximately reproduced the global evolution of HFC-152a as observed by the AGAGE network up to 2014. After 2014, we repeated the 2014 emission totals. We implemented loss to OH and ran one simulation with the prior OH fields from [9] and one with the optimized OH fields from the standard inversion. We found that when we reduced the emissions reported in [8] by 10%, which is well within their uncertainty bounds, the simulation best reproduced the global growth rate of HFC-152a.

Figure S3 shows site-to-site gradients of HFC-152a, as in Figure 5. We find that the gradients relative to the global mean mixing ratio, which we derived from the surface network using the same methods as for MCF, are largely insensitive to the emission totals we adopt. Given significant uncertainties in the emission distributions, it is expected that we do not capture all the gradients perfectly. However, we do

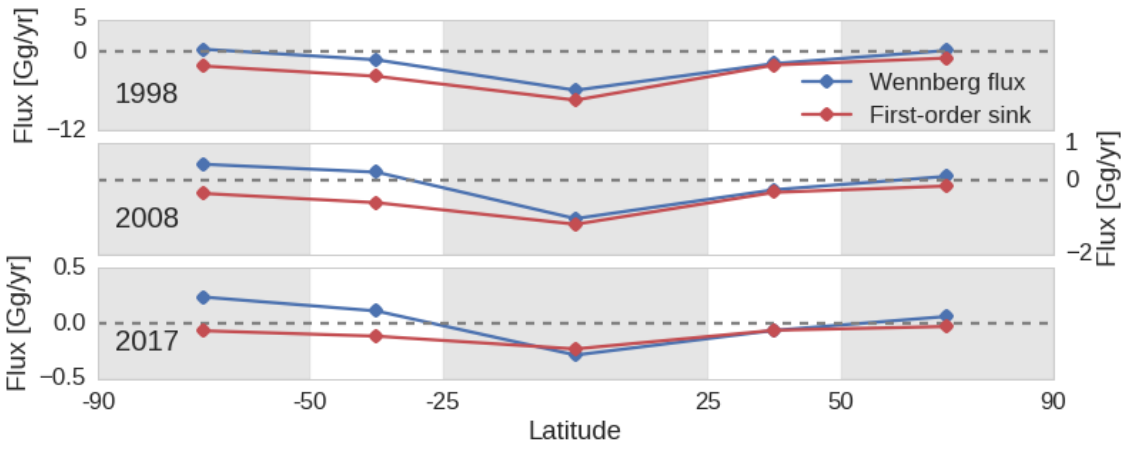

Figure S4: The latitudinal distribution of the annual total ocean flux from [10] and that of the first-order ocean sink from our posterior REF simulation, at three points in time. The fluxes are given for five latitudinal bands visualized in shaded areas. Fluxes are a function of ocean-atmosphere exchange rates and area covered by oceans in each latitudinal band.

expect that the SMO - CGO gradient is least sensitive to the emission distribution, and most sensitive to the OH distribution, under the assumption that it is unlikely that a large fraction of HFC-152a emissions is located in the Southern Hemisphere. Here, we see that the HFC-152a gradient between SMO and CGO is underestimated in the simulation with prior OH. This underestimate increases significantly if we impose the optimized OH fields. We note that the OH adjustments needed to fully correct for the biases in the simulations of MCF are even larger than the ones implemented here, which would deteriorate agreement with observed HFC-152a gradients even further.

We acknowledge that the HFC-152a budget is uncertain, as is its emission distribution [8] and we do not suggest that any underestimate of tropical OH is excluded with this HFC-152a analysis. However, an explanation that attributes the underestimate of intrahemispheric biases of MCF completely to an underestimate of tropical OH seems to be inconsistent with simulations of HFC-152a. Therefore, we conclude that the biases seem to a large degree specific to MCF, which makes it more likely that errors in the ocean-atmosphere exchange of MCF play a role (see Section 3.4).

S3 Ocean-atmosphere exchange of MCF in TM5

Figure S4 illustrates the latitudinal distribution of the Wennberg ocean flux at three points in time, compared to the first-order ocean sink used in our inversions. The absolute flux is largest and persistently negative in the tropics in both estimates, whereas at high latitudes the estimates diverge. Since the first-order ocean sink is based on optimized atmospheric mole fractions from the REF inversion, agreement in the tropics between the two estimates indicates that the forecasted MCF mole fractions in [10] were at least qualitatively realistic. For most of the period, the Wennberg ocean flux at high latitudes is positive, i.e. the oceans release MCF into the atmosphere. The difference at high latitudes is most pronounced in the Southern Hemisphere, mostly due to a larger ocean surface area. The latitudinal distribution of the Wennberg flux is somewhat time-variant, but persistently shows an enhanced latitudinal gradient compared to the first-order ocean sink over the 1998-2018 period. These observations are consistent with a relatively constant intrahemispheric bias that is higher in the Southern than in the Northern Hemisphere. For reference, the REF inversion found anthropogenic MCF emissions of 2.1 Gg in 2017, which can be compared to the 0.5 Gg difference between the Wennberg flux and the first-order sink in the Southern Hemisphere in the same year.

To test the potential impact on our derived results, we replaced the first-order ocean sink with the

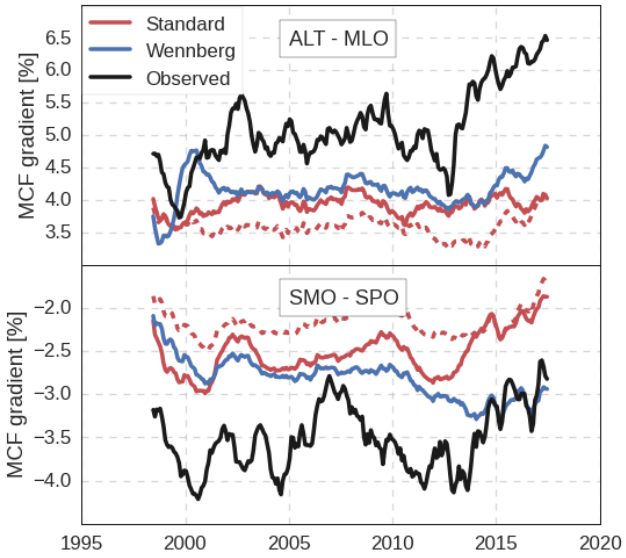

Figure S5: Simulated and observed MCF mole fraction gradients, treated analogous to Figure 5. Here, we compare the optimized (red solid) and prior (red dashed) gradients from the standard inversion to a forward simulation that includes the ocean-atmosphere exchange from [10].

Wennberg ocean flux in a forward simulation of MCF, while we kept the other fields the same as in the prior of the REF inversion. The effect on the intrahemispheric gradients of MCF is shown in Figure S5. For comparison, the prior and optimized simulations that result from the standard inversion are also shown. Predictably, adding MCF preferably at high latitudes compared to tropical latitudes deepens the tropical minimum of MCF. We find that this adjustment in the ocean sink provides strong leverage on the intrahemispheric gradient: implementation of the Wennberg flux improves the gradients more than the ∼30% adjustments in the latitudinal OH distribution that were derived in the REF inversion. Further implications of this result are discussed in Section 3.4.

While the air-sea exchange from [10] provides a viable alternative to a first-order sink, the estimated exchange does depend strongly on simulated ocean mixing. A second source of uncertainty are the oceanic hydrolysis rates. These rates are based on measurements performed at temperatures above 25°C, and were extrapolated to colder temperatures following the linear Arrhenius relation. While this relation was shown to hold at a range of temperatures above 25°C [11] [12], the only experiment performed at 10°C [13] provided much faster hydrolysis rates than those based on extrapolation. As concluded in [10], in-situ oceanic measurements of MCF would be needed to confirm and better constrain the oceanic release of MCF.

Based on these uncertainties, we emphasize that the actual air-sea exchange of MCF could differ significantly from [10]. Given the spatially similar signature of the proposed ocean sink and OH, we are unlikely to find tight constraints on both processes simultaneously in an inversion based on surface network observations. Partly for this reason, we choose not to further investigate the issue in additional inversions. However, we do find evidence in the underestimation of MCF intrahemispheric gradients that makes oceanic release of MCF more likely, even if we can't exactly quantify its magnitude. Such information is important for interpretation of the atmospheric MCF record.

S4 Ten year (1998-2008) inversions

In addition to the three twenty-year inversions, we performed three ten-year inversions, from 1998 to 2008. Since a ten-year inversion takes less time per iteration and the inverse problem is smaller, we found that the inversions converged more consistently and in fewer iterations. Considering the significant convergence

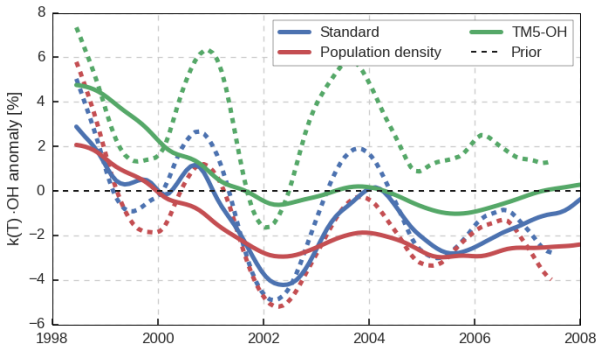

Figure S6: Monthly variations in global mean $k(T)$·OH, derived in the three different inversion set-ups. Solid lines indicate the results from inversions from 1998 to 2018: these are the same lines as those shown in Figure 1 of the main text. Dashed lines indicate the results from the ten-year inversions, which ran from 1998 to 2008.

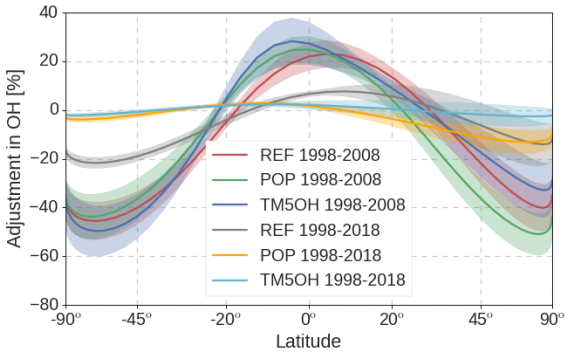

Figure S7: Adjustments made in the ten and twenty year inversions to the latitudinal distribution of OH. Annual mean adjustments were averaged over the 1998-2008 period, with colored bands quantifying spread between different years as one standard deviation. Note that the adjustment is shown relative to the prior, and that the REF and POP inversions use a different prior OH distribution than the TM5OH distribution.

problems we have found in the twenty-year inversions (see Section 3.5), this exercise served as a sanity check. In principle, if everything works correctly, then the twenty and ten-year inversions should converge to the same solution, excepting a spin-up and spin-down period.

Figure S6 shows the global k·OH variations derived from the ten and twenty-year inversions. It is clear that whereas there was quite some spread between the twenty-year inversions, the ten-year inversions converged to a similar solution that is most consistent with the standard twenty-year inversion. Similarly, the spatial adjustments in the OH distribution of the three ten-year inversions are very similar (Figure S7), even for the TM5-OH distribution, and in turn these adjustments are most similar in shape to the twenty-year REF inversion, although more extreme in amplitude.

In all cases, the ten-year inversions better reproduced MCF observations than the twenty-year inversions over the 1998-2008 time period. Mostly as a consequence of larger adjustments in the latitudinal OH distribution, the intrahemispheric gradients are reproduced better in the ten-year inversion, although still not quite captured (Figures S8). The inversion in which emissions were distributed according to population density (POP) consistently performs most poorly. Interestingly, the ten-year inversion that converges best uses an OH field based on a full-chemistry simulation of TM5, rather than the often-adopted distribution

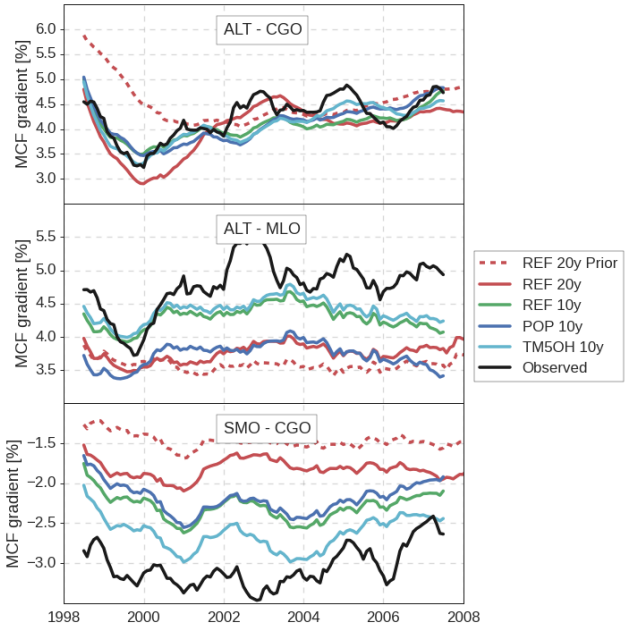

Figure S8: Simulated and observed MCF mole fraction gradients, treated analogous to Figure 5 in the main text. Here, we compare all three ten-year inversions and the REF inversion. We only show the prior gradient of the REF inversion (red dashed).

from [9]. However, this solution does require significantly elevated MCF emissions over the 1998-2008 period: a total of 21.4 Gg over ten years, or an average increase of 12.0 % relative to the prior. This increase is likely a consequence of relatively high OH concentrations in the Northern Hemisphere, so that higher MCF emissions are required to balance the interhemispheric gradient. Additionally, in the ten-year inversions, variations in MCF emissions and variations in OH adjustments do become significantly negatively correlated (typically $r = -0.6$), which was not the case for the twenty-year inversions. This indicates that the two cannot be fully disentangled at this level of detail.

By reducing the problem to one decade, we have more confidence that the inverse system managed to find a statistically correct solution than in the twenty-year inversion. This is supported by the consistency of the derived solutions. Since the solutions derived in the ten-year inversions most closely match the twenty-year REF inversion, we consider that the REF inversion managed to converge furthest. We are unsure why this particular inverse set-up managed to converge further than the other two. Notably, the interannual OH variations between the REF 20 year and 10 year inversions match quite well, except in 2006-2007, which can be considered spin-down years of the ten-year inversion. This lends confidence to this aspect of our twenty-year REF estimate. For the latitudinal adjustments in OH, it can be observed that more extreme adjustments result in incremental improvements in intrahemispheric gradients. I.e., given strong enough adjustments in the OH distribution, in combination with compensatory elevated MCF emissions, the intrahemispheric gradients can be reproduced. However, given the extremity of the necessary OH adjustments of at least 60% and the need for substantially increased emissions, we doubt the physical realism of this solution.

S5 The adjoint of OH chemistry

A 4DVAR inversion requires the adjoint of the forward version of TM5 to calculate the cost function gradient. The adjoint of TM5 has been described in previous publications [14] [15], here we describe the additions that are required for optimization of OH.

The adjoint of the forward model **H** is equivalent to the transpose of **H**, which is straightforward to find if **H** is linear. However, as loss to OH depends on both MCF mole fractions and OH, an adjustment in OH has a non-linear impact on loss of MCF. In that case, the adjoint is defined as the transpose of the tangent linear version of **H**. Equations 1 describe the forward OH chemistry in TM5.

$$\mathrm{MCF}(t+dt) = \mathrm{MCF}(t)\,(1 - k_{OH}\,\mathrm{OH}(t)), \tag{1a}$$
$$\mathrm{OH}(t+dt) = \mathrm{OH}(t). \tag{1b}$$

OH is the model OH concentration in molecules cm^{-3}, which does not vary within a month, dt is the model timestep in seconds and k_{OH} the reaction rate between MCF and OH in $\mathrm{cm}^3\ \mathrm{s}^{-1}$ $\mathrm{molecules}^{-1}$. The resulting tangent linear model, with respect to adjustments in OH, is given in Equations 2.

$$d\mathrm{MCF}(t+dt) = d\mathrm{MCF}(t)\,(1 - k_{OH}\,\mathrm{OH})(t) - \mathrm{MCF}\,k_{OH}\,d\mathrm{OH}(t), \tag{2a}$$
$$d\mathrm{OH}(t+dt) = d\mathrm{OH}(t). \tag{2b}$$

Since both MCF and OH are affected by OH adjustments, a non-linearity results. From the tangent linear model, the adjoint model can be derived and is given in Equations 3.

$$adj\mathrm{MCF}(t) = adj\mathrm{MCF}(t)\,(1 - k_{OH}\,\mathrm{OH}(t)) \tag{3a}$$
$$adj\mathrm{OH}(t) = adj\mathrm{OH}(t) - \mathrm{MCF}(t)\,k_{OH}\,adj\mathrm{MCF}(t). \tag{3b}$$

As in the forward model, the adjoint fields of MCF are 3-hourly, whereas the adjoint fields of OH are monthly. For the calculation of the adjoint of OH (Equation 3b), we need to save the 3-hourly, 3D MCF mole fraction fields from the forward run: effectively, we linearize around these fields. Note that if OH were not optimized, only Equation 3a would be needed.

Secondly, we need to translate between OH and scaling factors of OH. The conditional scaling of OH is defined in Equation 4.

$$\mathrm{OH}(t) = \begin{cases} \mathrm{OH}_{\mathrm{prior}}(t)\,(1 + f_{OH}(t)), & \text{if} f_{\mathrm{OH}} \geq 0, \\ \mathrm{OH}_{\mathrm{prior}}(t)\,\exp(f_{OH}(t)), & \text{if} f_{\mathrm{OH}} < 0, \end{cases} \tag{4}$$

with $\mathrm{OH}_{\mathrm{prior}}$ the monthly prior OH field and f_{OH} the monthly scaling factor that enters the state vector. Since $\mathrm{OH}_{\mathrm{prior}}$ is fixed, the only non-linearity comes from the exponent, and the tangent linear scaling becomes:

$$d\mathrm{OH}(t) = \begin{cases} \mathrm{OH}_{\mathrm{prior}}(t)\,df_{OH}(t), & \text{if} f_{OH} \geq 0, \\ \mathrm{OH}_{\mathrm{prior}}(t)\,df_{OH}(t)\,\exp(f_{OH}(t)), & \text{if} f_{OH} < 0. \end{cases} \tag{5}$$

Finally, the adjoint of the scaling factor can be described in terms of the adjoint field of OH as:

$$adj\mathrm{f}_{\mathrm{OH}}(t) = \begin{cases} \mathrm{OH}_{\mathrm{prior}}(t)\,adj\mathrm{OH}, & \text{if} f_{OH} \geq 0, \\ \mathrm{OH}_{\mathrm{prior}}(t)\,adj\mathrm{OH}\,\exp(f_{OH}(t)), & \text{if} f_{OH} < 0. \end{cases} \tag{6}$$

Aggregation of scaling factors per grid box to zones, e.g. over the longitudinal dimension, is done through summation. Emissions are scaled following an analogous version of Equations 4-6, as in [16].

S6 Tables

References

[1] S. Naus, S. A. Montzka, S. Pandey, S. Basu, E. J. Dlugokencky, and M. Krol. Constraints and biases in a tropospheric two-box model of OH. *Atmospheric Chemistry and Physics*, 19(1):407–424, 2019.

Site short	Location	Lat. (°)	Long. (°)	Alt. (m)	Measurement period
SPO	South Pole, Antarctica	-90.0	-24.8	2810	1992 − Present
PSA	Palmer Station, Antarctica	-64.9	-64.0	10	1997 − Present
CGO	Cape Grim, Tasmania, Australia	-40.7	144.7	164	1991 − Present
SMO	Tutuila, American Samoa, USA	-14.2	-170.6	42	1991 − Present
KUM	Cape Kumukahi, Hawaiï, USA	19.5	-154.8	8	1995 − Present
MLO	Mauna Loa, Hawaiï, USA	19.5	-155.6	3397	1991 − Present
NWR	Niwot Ridge, Colorado, USA	40.0	-105.6	3526	1991 − Present
THD	Trinidad Head, California, USA	41.0	-124.2	107	**2002** − Present
HFM	Harvard Forest, Massachusetts, USA	42.5	-72.2	340	1995 − Present
LEF	Park Falls, Wisconsin, USA	46.0	-90.3	472	1996 − Present
MHD	Mace Head, County Galway, Ireland	53.3	-9.9	26	1998 − Present
BRW	Barrow, Alaska, USA	71.3	-156.6	11	1992 − Present
SUM	Summit, Greenland	72.6	-38.5	3210	**2004** − 2018
ALT	Alert, Nunavut, Canada	82.5	-62.5	205	1991 − Present

Table S1: Description of the NOAA surface sites used in this study. Shown are abbreviation, full name and location, latitude, altitude and longitude, and the start and end year of measurements at a site. The instances where a site does not cover the full inversion period are shown in bold.

[2] T. Kovács, W. Feng, A. Totterdill, J. M. C. Plane, S. Dhomse, J. C. Gómez-Martín, G. P. Stiller, F. J. Haenel, C. Smith, P. M. Forster, R. R. García, D. R. Marsh, and M. P. Chipperfield. Determination of the atmospheric lifetime and global warming potential of sulfur hexafluoride using a three-dimensional model. *Atmospheric Chemistry and Physics*, 17(2):883–898, 2017.

[3] I. Levin and V. Hesshaimer. Refining of atmospheric transport model entries by the globally observed passive tracer distributions of ^{85}krypton and sulfur hexafluoride (SF_6). *Journal of Geophysical Research: Atmospheres*, 101(D11):16745–16755, 1996.

[4] M. Gloor, E. Dlugokencky, C. Brenninkmeijer, L. Horowitz, D. F. Hurst, G. Dutton, C. Crevoisier, T. Machida, and P. Tans. Three-dimensional SF6 data and tropospheric transport simulations: Signals, modeling accuracy, and implications for inverse modeling. *Journal of Geophysical Research: Atmospheres*, 112(D15), 2007.

[5] M. Krol, M. de Bruine, L. Killaars, H. Ouwersloot, A. Pozzer, Y. Yin, F. Chevallier, P. Bousquet, P. Patra, D. Belikov, S. Maksyutov, S. Dhomse, W. Feng, and M. P. Chipperfield. Age of air as a diagnostic for transport timescales in global models. *Geoscientific Model Development*, 11(8):3109–3130, 2018.

[6] M. K. W. Ko, P. A. Newman, S. Reimann, and S.E. (Eds.) Strahan. SPARC report on the lifetimes of stratospheric ozone-depleting substances, their replacements, and related species. *SPARC Report No. 6*, 2013.

[7] Q. Liang, M. P. Chipperfield, E. L. Fleming, N. L. Abraham, P. Braesicke, J. B. Burkholder, J. S. Daniel, S. Dhomse, P. J. Fraser, S. C. Hardiman, et al. Deriving Global OH Abundance and Atmospheric Lifetimes for Long-Lived Gases: A Search for CH_3CCl_3 Alternatives. *Journal of Geophysical Research: Atmospheres*, 2017.

[8] P. G. Simmonds, M. Rigby, A. J. Manning, M. F. Lunt, S. O'Doherty, A. McCulloch, P. J. Fraser, S. Henne, M. K. Vollmer, J. Mühle, R. F. Weiss, P. K. Salameh, D. Young, S. Reimann, A. Wenger,

T. Arnold, C. M. Harth, P. B. Krummel, L. P. Steele, B. L. Dunse, B. R. Miller, C. R. Lunder, O. Hermansen, N. Schmidbauer, T. Saito, Y. Yokouchi, S. Park, S. Li, B. Yao, L. X. Zhou, J. Arduini, M. Maione, R. H. J. Wang, D. Ivy, and R. G. Prinn. Global and regional emissions estimates of 1,1-difluoroethane (HFC-152a, CH_3CHF_2) from in situ and air archive observations. *Atmospheric Chemistry and Physics*, 16(1):365–382, 2016.

[9] C. M. Spivakovsky, J. A. Logan, S. A. Montzka, Y. J. Balkanski, M. Foreman-Fowler, D. B. A. Jones, L. W. Horowitz, A. C. Fusco, C. A. M. Brenninkmeijer, M. J. Prather, et al. Three-dimensional climatological distribution of tropospheric OH: Update and evaluation. *Journal of Geophysical Research: Atmospheres*, 105(D7):8931–8980, 2000.

[10] P. O. Wennberg, S. Peacock, J. T. Randerson, and R. Bleck. Recent changes in the air-sea gas exchange of methyl chloroform. *Geophysical research letters*, 31(16), 2004.

[11] R. R. Gerkens and J. A. Franklin. The rate of degradation of 1, 1, 1-trichloroethane in water by hydrolysis and dehydrochlorination. *Chemosphere*, 19(12):1929–1937, 1989.

[12] P. M. Jeffers, L. M. Ward, L. M. Woytowitch, and N. L. Wolfe. Homogeneous hydrolysis rate constants for selected chlorinated methanes, ethanes, ethenes, and propanes. *Environmental Science & Technology*, 23(8):965–969, 1989.

[13] C. R. Pearson and G. McConnell. Chlorinated C_1 and C_2 hydrocarbons in the marine environment. *Proceedings of the Royal Society of London. Series B. Biological Sciences*, 189(1096):305–332, 1975.

[14] J. F. Meirink, P. Bergamaschi, and M. C. Krol. Four-dimensional variational data assimilation for inverse modelling of atmospheric methane emissions: method and comparison with synthesis inversion. *Atmospheric chemistry and physics*, 8(21):6341–6353, 2008.

[15] M. C. Krol, J. F. Meirink, P. Bergamaschi, J. E. Mak, D. Lowe, P. Jöckel, S. Houweling, and T. Röckmann. What can ^{14}CO measurements tell us about OH? *Atmospheric chemistry and physics*, 8(16):5033–5044, 2008.

[16] P. Bergamaschi, C. Frankenberg, J. F. Meirink, M. Krol, M. G. Villani, S. Houweling, F. Dentener, E. J. Dlugokencky, J. B. Miller, L. V. Gatti, A. Engel, and I. Levin. Inverse modeling of global and regional CH_4 emissions using SCIAMACHY satellite retrievals. *Journal of Geophysical Research: Atmospheres*, 114(D22), 2009.